Sensors and Actuators A 208 (2014) 37–49

Contents lists available at ScienceDirect

Sensors and Actuators A: Physical

journal homepage: www.elsevier.com/locate/sna

Micromachined ultrasonic Doppler velocity sensor using nickel on glass transducers

Minchul Shin[a], Zhengxin Zhao[a], Paul DeBitetto[b], Robert D. White[a,*]

[a] Mechanical Engineering, Tufts University, 200 College Avenue, Medford, MA 02155, USA
[b] Draper Laboratory, 555 Technology Square, Cambridge, MA 02139, USA

ARTICLE INFO

Article history:
Received 5 August 2013
Received in revised form 2 December 2013
Accepted 16 December 2013
Available online 3 January 2014

Keywords:
Micromachined
Ultrasound
Doppler
Velocity
Sensor
Array

ABSTRACT

A micromachined array of 168 nickel-on-glass capacitive ultrasound transducers was used to demonstrate a long range Doppler velocity measurement system. By using an electroplated nickel on glass process, the total capacitance of the chip was reduced to 65 pF, resulting in a high signal to noise ratio and allowing an operable range of 1.5 m. The range is limited by room reverberation level, rather than electronic noise. The sensor array operates at a 180 kHz resonant frequency to achieve a half-angle −3 dB beamwidth of 6° with a 1 cm^2 die. The cMUT array was characterized using laser Doppler vibrometry (LDV), beampattern measurements, range testing, and the ability to measure the velocity of a moving plate. The sensor is capable of measuring the velocity of a moving reflector with a resolution of 6 cm/s, at an update rate of 0.016 s, and with a range of 1.5 m (3 m round trip).

1. Introduction

Range finding and velocity measurement sensors are required for a variety of navigation tasks including mobile robot navigation, personal navigation systems, automotive sensing, micro air vehicle navigation, obstacle detection, and map building [1–6]. A number of possible sensing modalities exist, including millimeter wave RADAR systems, laser range finding systems, and infrared range finding systems. Ultrasonic range finding and velocity measurement is also an option with certain advantages.

Among suitable techniques, RADAR-based Doppler velocity or distance measurement systems and laser rangefinders can provide high accuracy. However, these systems suffer from high power consumption and high cost. Laser rangefinders may also be sensitive to ambient light conditions, and may not be able to penetrate heavy rain or snow [7,8,27]. When compared with an ultrasonic array of high enough frequency (e.g. 180 kHz as described here), millimeter wave RADAR tends to require a larger aperture to provide a narrow beam, resulting in a physically large system. For instance, a modern automotive millimeter wave RADAR system operating at $f = 77$ GHz [27] with a desired half-angle beamwidth of $\theta = 6°$, would require an aperture of $L \approx 3.7$ cm [32, p. 192],

$$L \approx \frac{c/f}{\sin\ \theta} \tag{1}$$

Eq. (1) is valid for acoustic and RF waves. Hence, due to the much lower speed of sound as compared to RF, the same beamwidth can be achieved at 180 kHz, as done in the ultrasonic device described here, with a 1 cm aperture. Another approach for obstacle detection in mobile robotics is infrared reflectance sensors. These devices tend to be low cost and low power consumption. However, the infrared rangefinder tends to have low accuracy, and may suffer from ambient light sensitivity and sensitivity to surface characteristics [8,9].

Ultrasonic sensors are another alternative for navigation and obstacle detection. They have advantages of low cost, small size, low power consumption, and simple signal processing [10]. Ultrasound will scatter and absorb in a different manner than lasers and IR, if for no other reason than the difference in wavelength (millimeters vs. hundreds of nanometers or a few microns). In addition, it will scatter and absorb differently than millimeter RADAR, despite the similar wavelength, due to the different wave modality (acoustic rather than electromagnetic). Thus, due to their low cost, size, and power, as well as the additional environmental information they provide, ultrasonic sensors are an

* Corresponding author. Tel.: +1 617 627 2210.
E-mail address: r.white@tufts.edu (R.D. White).

0924-4247/$ – see front matter © 2013 Elsevier B.V. All rights reserved.
http://dx.doi.org/10.1016/j.sna.2013.12.025

attractive sensor technology to include in a mix of navigational sensors. It is, however, important to note that ultrasonic sensors also can suffer from the drawback of multipath reflections, which can result in poor distance measurements, and may also be sensitive to changes in reflecting surfaces and ambient conditions.

Ultrasonic distance measurement systems are available commercially, although they typically operate at frequencies near 40 kHz. Some examples include the well-known Polaroid ranging module that uses a time of flight distance measurement method and operates at frequencies between 49 and 60 kHz [24]. Another example is the SRF series ultrasonic sensor from Devantech [Devantech, Norfolk, England] which is smaller than the Polaroid system, with a 4.3 cm × 2 cm front aperture. This system operates at 40 kHz. For a 1 cm aperture transducer, the size used for the device described in this paper, a frequency of 40–60 kHz results in a half-angle beamwidth of 35–60°, according to Eq. (1). Hence the sensors are not very directional, contributing to problems with reverberation and multipath reflections.

It is, however, expected that a more directional sensor will generate, and pick up, fewer multipath echoes. Through the use of MEMS technology, the operating frequency can be increased to 180 kHz, as demonstrated here, and thus the half-angle beamwidth can be reduced from 35–60° to 6°, resulting in substantially improved directionality. The increase in frequency reduces the range of the sensor to some degree due to the increase in bulk absorption at higher frequencies, but the range can still be kept acceptably high.

MEMS based ultrasonic sensor systems including both piezoelectric micromachined ultrasound transducers (pMUTs) and capacitive micromachined ultrasound transducers (cMUTs) have been described for other applications previously [e.g. 16, 22, 25, 26, 29, 31, 33, 35], with a preponderance of applications in biomedical ultrasound and non-destructive testing. A few authors [10,11,38,40] have described MEMS-based ultrasonic distance measurement systems. These systems use either piezoelectric or thermal actuation principles, and achieve a range of 10 cm to, at most, 1.3 m.

Indeed, although MEMS-based rangefinders have the advantage of low cost and high portability with a small size, they must overcome challenges in terms of power output and sensitivity that can result in a limited range [11]. For example, a previous system, described by the authors, which used polysilicon surface micromachined cMUTs only achieved a 30 cm (60 cm round trip) range [38]. To overcome the short-range problem, the cMUT device described here was developed with a low stray capacitance and a high drive voltage drive. This combination allowed an achievable range to the reflector of 1.5 m (3 m round trip).

The device described in this paper is fabricated in a 3 layer nickel-on-glass MEMS fabrication process for cMUT sensors that was critical for achieving low stray capacitance. The low capacitance is achieved due to the complete lack of a conducting or semiconducting substrate below the signal traces and bond pads; by using a dielectric (glass) substrate, stray capacitance between traces and bond pads is dramatically reduced when compared to a device built on a semiconducting substrate with a thin layer dielectric. This process has some similarities to LIGA and LIGA-like processing [12–15] but is considerably simpler to implement. The process enables fabrication for the production of a range of low stray capacitance sensors; for instance we have used this process for shear sensors [21]. This paper outlines the methods for creating a solution for a smaller, lower cost, low capacitance, long range, and low power MEMS ultrasonic array for velocity measurement in air. This is the only example in the literature of a cMUT based ultrasonic velocity measurement system in air with a range of more than 30 cm.

2. Design and modeling

The transducer array consists of 168 individual array elements arranged in a 14 × 12 hexagonal grid on a 1 cm^2 chip. The transmit area of the array is 9 mm × 9 mm. The 1 cm size of the chip, which sets the array aperture, was selected to give the same beamwidth as typical automotive millimeter wave RADAR systems (6°) at an achievable operating frequency (180 kHz) [27]. Aperture and operating frequency can be modified to change beamwidth according to Eq. (1), within constraints of system size and achievable resonant frequency.

The individual elements are 600 μm diameter, 9 μm thick Nickel, separated from a 390 μm diameter Cr/Au bottom electrode by a 5 μm air gap. Element diameter was selected to be significantly less than the wavelength of sound at the 180 kHz operating frequency (at 180 kHz, λ = 1.9 mm), but to be as large as possible (which maximizes signal) without collapsing due to in-process adhesion related failure (e.g. stiction). The elements were packed as closely together as possible in order to maximize signal. Due to the geometry of a hexagonal close packed array, adjacent rows are spaced 0.72 mm center-to-center, and adjacent columns are spaced 0.63 mm center-to-center. Since the element motion is larger near the center than the edge, the center of the electrode contributes more signal than the outside of the electrode. However, both center and edge contribute the same amount of stray capacitance. Thus, it is beneficial to use an electrode that is somewhat smaller than the diaphragm, in order to improve sensitivity. The exact size was not optimized. Twenty-eight 10 μm diameter vent holes are included in each diaphragm for release etching and static pressure equalization. The vent holes also control the damping. All elements are connected in parallel. The geometry is shown in Fig. 1.

A fully coupled electro-acoustic-mechanical model was constructed for the system. The model is similar to that described previously for other MEMS cMUTs [16,38]. The model includes the diaphragm stiffness and mass, including residual stress effects, squeeze film damping, backing cavity compliance, vent hole damping, and external air impedance. The acoustic-mechanical model is coupled in a bi-directional fashion to the electrical domain via electrostatic coupling. Fig. 2 shows the geometry and an equivalent acoustic circuit for the model.

The model derivation begins from the equation for a thin bending plate with residual stress, forced by distributed pressures from the electrostatics and the air,

$$D\nabla^4 u(r,t) - T\nabla^2 u(r,t) + \rho_{Ni} h \frac{\partial^2 u(r,t)}{\partial t^2} = \frac{1}{2} V^2(t) \frac{\varepsilon_0}{(g_0 - u(r,t))^2} \Phi(a_2 - r) + p_1(t) - p_2(t) \quad (2)$$

where r is the radial coordinate, t is time, $u(r,t)$ is the displacement of the diaphragm, positive downwards, $V(t)$ is the applied voltage, $p_1(t)$ and $p_2(t)$ are the pressures above and below the diaphragm, ε_0 is the permittivity of free space, g_0 is the gap height (5 μm), ρ_{Ni} is the density of Nickel, taken to be 8900 kg/m^3 [17], and h is the thickness of the diaphragm (9 μm). It is assumed that the pressure in the gap and the pressure in the external acoustic medium are nearly constant with radial position, since for the frequencies of interest, near 180 kHz, the wavelength of sound, λ = 1.9 mm, is greater than the radius of the diaphragm, a_1 = 0.3 mm. The electrostatic force only acts over the area of the electrode, which is a circle of radius a_2. Thus the Heaviside step function $\Phi(a_2 - r)$ appears on the right. D and T are the bending stiffness and tension, respectively,

$$D = \frac{Eh^3}{12(1-\nu^2)} \quad (3)$$

$$T = \sigma_R h \quad (4)$$

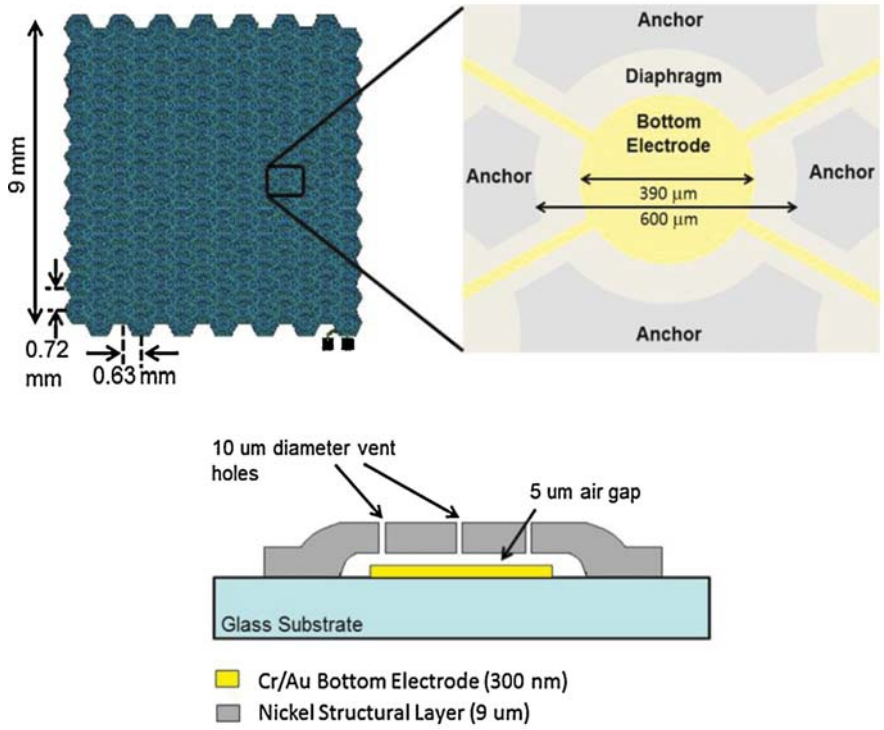

Fig. 1. Transducer geometry. Top left: full array chip. Top right: individual element, top view. Bottom: individual element, cross-section.

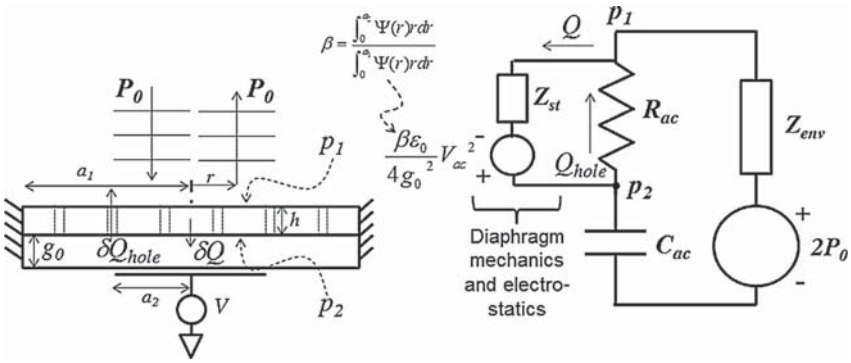

Fig. 2. Electro-acoustic-mechanical model of a single axisymmetric element.

Table 1
Geometric properties of the nickel-on-glass cMUT sensor.

Symbol	Property	Value	Units
a_1	Radius of diaphragm	300	μm
a_2	Radius of bottom electrode	195	μm
h	Thickness of nickel layer	9	μm
g_0	Thickness of sacrificial layer (air gap)	5	μm
r_1	Radius of diaphragm vent holes	5	μm
N	Number of vent holes in diaphragm	28	Dimensionless

where E and ν are the elastic modulus and Poisson ratio of the electroplated Nickel, taken to be 205 GPa and 0.31 [18,19] and σ_R is the residual stress in the Nickel film. The residual stress for plated nickel thin films prepared from nickel sulfamate plating baths can vary considerably, from at least −80 MPa to +80 MPa, depending on additives, plating temperature, current density, and film thickness [e.g. 36]. Summaries of the geometric and material properties for the model appear in Tables 1 and 2.

Steady state harmonic solutions with time variation $e^{j\omega t}$ are sought. For receive operation, the bias is held constant, $V(t) = V_{dc}$.

Table 2
Material properties of the diaphragm.

Symbol	Property	Value	Units	Reference(s)
ρ_{Ni}	Density of nickel	8900	kg/m^3	[17]
E	Modulus of elasticity of nickel	205	GPa	[18]
σ_R	Residual stress of nickel	−80 to 80	MPa	[36]
ν	Poisson's ratio of nickel	0.31	Dimensionless	[19]

For transmit operation the applied voltage is harmonic at ω_{ac}, $V(t) = V_{ac}\cos(\omega_{ac}t)$. In transmit mode, this will produce a primary steady state response at $\omega = 2\omega_{ac}$ due to the square law electrostatics. A Galerkin procedure can be employed to determine $u(r)$ [42–44]. A functional form is assumed that satisfies the boundary conditions with an unknown coefficient or coefficients:

$$u(r) = U_0\Psi(r) \tag{5}$$

where U_0, in this case, is the unknown centerpoint displacement. After substitution of Eq. (5) for $u(r)$ in Eq. (2), multiplication of both sides of Eq. (2) by $u(r)$, and integration over the domain, a result is arrived at for U_0,

$$U_0 = \left[D\frac{\int_0^{a_1}\Psi(r)\nabla^4\Psi(r)rdr}{\int_0^{a_1}\Psi(r)rdr} - T\frac{\int_0^{a_1}\Psi(r)\nabla^2\Psi(r)rdr}{\int_0^{a_1}\Psi(r)rdr} - h\rho_{Ni}\omega^2\frac{\int_0^{a_1}\Psi^2(r)rdr}{\int_0^{a_1}\Psi(r)rdr} - \frac{\varepsilon_0}{g_0^3}\left(V_{dc}^2 + \frac{V_{ac}^2}{2}\right)\frac{\int_0^{a_2}\Psi^2(r)rdr}{\int_0^{a_1}\Psi(r)rdr}\right]^{-1} \cdot \left(\frac{\int_0^{a_2}\Psi(r)rdr}{\int_0^{a_1}\Psi(r)rdr}\frac{\varepsilon_0}{4g_0^2}V_{ac}^2 + (p_1 - p_2)\right) \tag{6}$$

This result can be used to determine the structural acoustic impedance in Fig. 2, where the volume velocity of the diaphragm is driven by the differential pressure and the effective electrostatic pressure:

$$Q = \frac{1}{Z_{st}}\left(\frac{\int_0^{a_2}\Psi(r)rdr}{\int_0^{a_1}\Psi(r)rdr}\frac{\varepsilon_0}{4g_0^2}V_{ac}^2 + (p_1 - p_2)\right) \tag{7}$$

where Q is the oscillatory volume velocity of the diaphragm,

$$Q = 2\pi j\omega\int_0^{a_1}u(r)rdr \tag{8}$$

Thus Q can be related to the centerpoint displacement by

$$U_0 = \frac{Q}{2\pi j\omega\int_0^{a_1}\Psi(r)rdr} \tag{9}$$

Then, from Eqs. (6) and (7), the structural impedance can be determined,

$$Z_{st} = h\rho_{Ni}\frac{\int_0^{a_1}\Psi^2(r)rdr}{2\pi\left(\int_0^{a_1}\Psi(r)rdr\right)^2}j\omega + \left[D\frac{\int_0^{a_1}\Psi(r)\nabla^4\Psi(r)rdr}{2\pi\left(\int_0^{a_1}\Psi(r)rdr\right)^2} - T\frac{\int_0^{a_1}\Psi(r)\nabla^2\Psi(r)rdr}{2\pi\left(\int_0^{a_1}\Psi(r)rdr\right)^2} - \frac{\varepsilon_0\int_0^{a_2}\Psi^2(r)rdr}{g_0^3 2\pi\left(\int_0^{a_1}\Psi(r)rdr\right)^2}\left(V_{dc}^2 + \frac{V_{ac}^2}{2}\right)\right]\frac{1}{j\omega} \tag{10}$$

The impedance shows a mass in series with a stiffness, as expected. The negative stiffness of the electrostatic spring is evident in the last term. The result will only be valid up through the first resonant frequency, above which the assumed modeshape will no longer be valid. The structural impedance can be written as

$$Z_{st} = M_{st}j\omega + \frac{1}{C_{st}j\omega} + \frac{1}{C_{el}j\omega} \tag{11}$$

where C_{st} is the structural compliance for the first mode, C_{el} is the effective linearized electrostatic spring compliance, and M_{st} is the structural mass for the first mode. From (10) and (11) it is seen that

$$M_{st} = h\rho_{Ni}\frac{\int_0^{a_1}\Psi^2(r)rdr}{2\pi\left(\int_0^{a_1}\Psi(r)rdr\right)^2} \tag{12}$$

$$C_{st} = \left[D\frac{\int_0^{a_1}\Psi(r)\nabla^4\Psi(r)rdr}{2\pi\left(\int_0^{a_1}\Psi(r)rdr\right)^2} - T\frac{\int_0^{a_1}\Psi(r)\nabla^2\Psi(r)rdr}{2\pi\left(\int_0^{a_1}\Psi(r)rdr\right)^2}\right]^{-1} \tag{13}$$

$$C_{el} = -\left[\frac{\varepsilon_0\int_0^{a_2}\Psi^2(r)rdr}{g_0^3 2\pi\left(\int_0^{a_1}\Psi(r)rdr\right)^2}\left(V_{dc}^2 + \frac{V_{ac}^2}{2}\right)\right]^{-1} \tag{14}$$

In order to compute the structural impedance and the electrostatic coupling, a deflection shape, $\Psi(r)$, must be selected. Results will be shown below for a few different possible choices of shape. The integrals can be performed analytically or numerically.

The pressures above and below the diaphragm, p_1 and p_2, are computed from the acoustic circuit in Fig. 2. The acoustic capacitance represents the compressibility of the air in the gap [23],

$$C_{ac} = \frac{g_0\pi a_1^2}{\rho_0 c^2} \tag{15}$$

For flow in a thin gap below an oscillating perforated plate, the flow resistance including squeeze film damping and viscous flow resistance through the holes can be approximated as [30],

$$R_{ac} = \frac{12\mu}{\pi g_0^3 N}C(A) + \frac{8\mu}{\pi r_1^4 N}\left(h + \frac{3\pi r_1}{8}\right) \tag{16}$$

The first term comes from "squeeze film" resistance to flow in the gap behind the diaphragm. The second term represents the resistance to flow through the holes in the diaphragm. r_1 is the radius of the vent holes, N is the number of holes in the diaphragm, and μ is the viscosity of air, taken to be 1.85×10^{-5} Pa s. The parameter $C(A)$ is

$$C(A) = \frac{A}{2} - \frac{3}{8} - \frac{A^2}{8} - \frac{1}{2}\ln(\sqrt{A}) \tag{17}$$

where $A = Nr_1^2/a_1^2$ is the ratio of the hole area to the full diaphragm area. The result is identical to Škvor's formula [39].

The complex acoustic pressure on the top surface of the diaphragm comes from a combination of any incoming pressure wave and the pressure generated by the oscillating element acting as an acoustic source. The net velocity that creates the acoustic source is the difference between the velocity through the holes and the velocity of the diaphragm itself, as indicated by the topology of the acoustic circuit. The pressure on the top surface of the diaphragm is therefore

$$p_1 = Z_{env}\cdot(Q_{hole} - Q) + 2P_0 \tag{18}$$

The term P_0 represents an incoming acoustic plane wave. This is included to model an external acoustic input coming from the environment in "receive" mode. The factor of 2 comes from the scattered rigid wave. In transmit mode, $P_0 = 0$.

The environmental impedance can be estimated from the radiation impedance of a clamped circular diaphragm oscillating in the static bending modeshape. The environmental impedance has been derived by Greenspan [28],

$$Z_{env} \approx \frac{\rho_0 c}{a_1^2}\left(\frac{1}{2\pi}(ka_1)^2 + 0.296j(ka_1)\right) \tag{19}$$

c is the speed of sound, taken to be 343 m/s, and ρ_0 is the equilibrium density of the acoustic medium, taken to be 1.21 kg/m^3. This

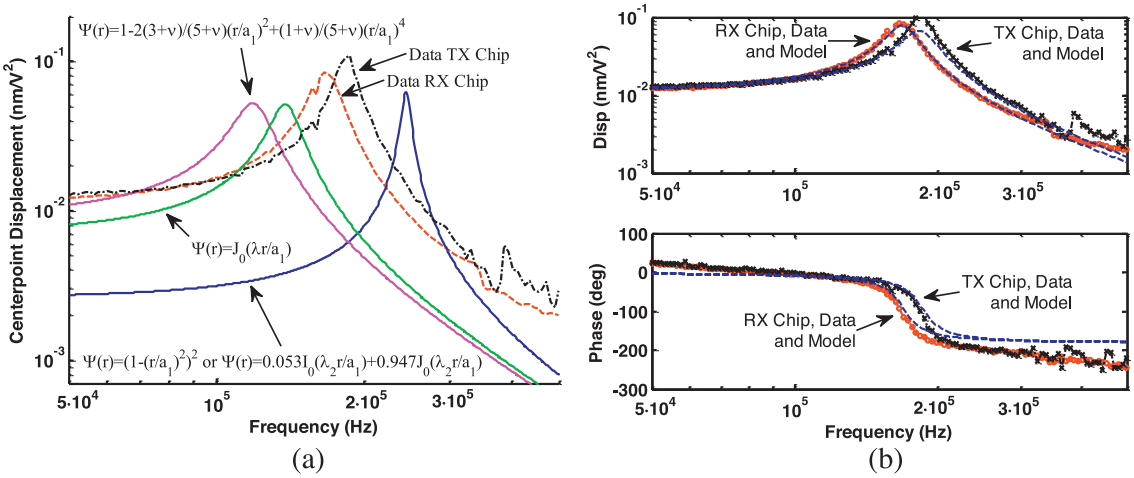

Fig. 3. Comparison between the measured center point vibratory response for the transmit (TX) and receive (RX) chips, and the predictions from the model. (a) Shows the magnitude results for four different possible choices of shape function and with zero residual stress. (b) Shows the comparison using the best fit values of structural impedance given in Table 3.

is a good approximation for $ka_1 < 0.5$. At low frequencies this is an acoustic mass in parallel with an acoustic radiation resistance. An extensive discussion of the computation of the radiation impedance of circular diaphragms including multiple possible modeshapes and extending to higher frequencies can be found in Lax [34], Porter [37], and Greenspan [28]. For this device there is not much to be gained by more complicated environmental impedance models. The environmental impedance has little impact on device dynamics. This would not, however, be the case for a water loaded device, where environmental impedance would have a much more significant impact.

All the impedances in the acoustic circuit have been defined. Using elementary circuit theory, the volume velocities Q and Q_{hole} can be computed in terms of the external driving pressure P_0 in receive mode, or the AC drive voltage V_{ac} in transmit mode. Once Q and Q_{hole} are known, the magnitude of the oscillatory centerpoint deflection can be computed from Eq. (9).

A direct comparison of model predictions can be made to the diaphragm center point oscillation measured using a laser Doppler velocimetry (LDV) system. In this experiment, the diaphragm is driven by an AC voltage of amplitude V_{ac} with an applied DC bias, resulting in an electrostatic force at the same frequency as the AC drive. For this type of excitation, the driving V_{ac}^2 in the voltage source should be replaced with $4\,V_{dc}V_{ac}$. Otherwise the model is unchanged. In Fig. 3, the predicted center point displacement from the dynamic model is compared to the measured center point response for an element on each of the two chips. The data is normalized to the product of the applied DC bias of 9 V and the applied AC peak drive of 1 V.

In Fig. 3(a) model predictions are shown for the following possible shape functions, with an assumed residual stress of zero. The measured LDV response of the two chips is also shown. All choices of shape produce predictions of center frequency and peak response that are within a factor of 2 of the measured result, but with the unknown residual stress and lack of certainty about the best choice of shape function, uncertainties remain in model predictions prior to performing dynamic experiments. The shapes used in Fig. 3(a) are: the response of an axisymmetric circular bending plate with a clamped edge to a uniform static pressure load [41, p. 178],

$$\Psi(r) = \left(1 - \left(\frac{r}{a_1}\right)^2\right)^2 \tag{20}$$

the response of an axisymmetric circular bending plate with a simply supported edge to a uniform static pressure load [41, p. 168],

$$\Psi(r) = 1 - 2\frac{3+\nu}{5+\nu}\left(\frac{r}{a_1}\right)^2 + \frac{1+\nu}{5+\nu}\left(\frac{r}{a_1}\right)^4 \tag{21}$$

the first in vacuo vibratory mode of a circular tensioned membrane [32],

$$\Psi(r) = J_0\left(2.4048\frac{r}{a_1}\right) \tag{22}$$

and the first in vacuo vibratory mode of a circular plate with clamped edges [34],

$$\Psi(r) = 0.0528I_0\left(3.196\frac{r}{a_1}\right) + 0.9472J_0\left(3.196\frac{r}{a_1}\right) \tag{23}$$

Due to uncertainties in the nickel residual stress and boundary conditions, it is unclear which of these choices will give the most accurate result. For low stress (pure bending) at low frequencies, Eq. (20) or Eq. (21), should work well, depending on the flexibility of the anchors, and therefore the best choice of boundary condition. For high stress (tension dominated) near resonance, Eq. (22) is expected to be a good choice. For low stress (bending dominated) near resonance, Eq. (23) may produce superior results. Any of these shapes can be used to predict an approximate frequency response curve, as shown in Fig. 3(a). This is very useful for targeting the design to approximately achieve a desire center frequency, gain, and bandwidth. By testing multiple shapes we also achieve a sense of expected levels of variation due to changes in residual stress and boundary conditions. Typically, we find that exactly matching the model to the dynamic response of the system can only be done after fitting at least one parameter using experimental data. It is then possible to iterate on the design using the fitted parameter to achieve a closer match to a target operating point. Alternatively, one could solve Eq. (2) numerically at a series of frequencies. This will require selection of boundary conditions and estimation of residual stress, as well as estimation of the relative magnitude of the pressure and electrostatic driving terms on the right hand side. The resulting solutions could be used as a frequency dependent $\Psi(r)$, resulting in frequency dependent structural impedances. However, due to uncertainties in the residual stress and boundary conditions, and variation in film properties from wafer to wafer or chip to chip, these impedances will still not exactly match experimental results.

Table 3
Structural impedance of the diaphragm as computed from Eqs. (12) and (13) with $\sigma_R = 0$ MPa with $\Psi(r) = J_0(2.4048\, r/a_1)$, and compared to the best fit values for fitting the LDV data in Fig.3.

	Analytical result, $\sigma_R = 0$, $\Psi(r) = J_0(2.4048 \cdot r/a_1)$	Best fit RX	Best fit TX
C_{st}	3.4×10^{-18} m^3/Pa	3.8×10^{-18} m^3/Pa	3.8×10^{-18} m^3/Pa
M_{st}	4.1×10^{5} kg/m^4	2.6×10^{5} kg/m^4	2.2×10^{5} kg/m^4

Once dynamic data is available, the best option for predicting the acoustic response is to determine the structural compliance and mass, C_{st} and M_{st}, by fitting the measured response for each chip. The model is still physics based, but the structural uncertainties have been removed by fitting to data. Fig. 3(b) shows a comparison to the data with these best fit values. The best fit values of C_{st} and M_{st} are given in Table 3, and compared for interest to the results using the first in vacuo tensioned membrane mode of Eq. (22) with zero residual stress. For subsequent computations, the best fit values of C_{st} and M_{st} will be used.

The farfield transmitted pressure from the array can be computed at any point in the field (r_f, θ_f, ϕ_f) by summing the contribution from each element in the array treated individually as a directional source,

$$P(r_f, \theta_f, \phi_f) = \frac{j\rho_0\omega}{2\pi} \cdot \sum_{m=1}^{N} \frac{1}{R_m} \cdot (Q_{\text{hole}} - Q) e^{(-\alpha_c - jk)R_m} H(\theta_f) \tag{24}$$

where $Q_{hole} - Q$ is the net source volume velocity: the difference between the diaphragm volume velocity and the flow through the vent holes. R_m is the scalar distance from the center of the mth array element to the field point. $H(\theta_f)$ is the directivity of an individual element. The acoustic absorption is α_c in Np/m. At frequencies near 180 kHz in air of this is well modeled using the classical absorption coefficient [32],

$$\alpha_c = \frac{\omega^2 \mu}{2\rho_0 c^3} \left(\frac{4}{3} + \frac{\gamma - 1}{Pr} \right) = \left(1.37 \times 10^{-11} \frac{Np \cdot s^2}{m} \right) f^2 \tag{25}$$

where $\gamma = 1.40$ is the ratio of specific heats for air near 20 °C, and $Pr = 0.75$ is the Prandtl number of air near 20 °C. f is the frequency in Hz.

At the drive frequency of 180 kHz, ka_1 is close to unity, so the individual elements are somewhat directional. The beampattern of a baffled piston is used to approximate the beampattern of the individual elements,

$$H(\theta_f) = \frac{2J_1(ka_{eff} \sin \theta_f)}{ka_{eff} \sin \theta_f} \tag{26}$$

where θ is the angle, measured from the normal to the field point, and J_1 is the Bessel function of the first kind, order 1. For the purposes of directivity calculation, the effective radius, a_{eff}, of the transmitting element should be used. Since the element deforms as a circular bending plate, the effective radius of an equivalent baffled piston is somewhat less than the physical radius. An effective radius equal to 70% of the physical radius is a good approximation. This was determined by a comparing Eq. (26) to a numerical computation of the farfield beampattern for a baffled circular plate oscillating in the clamped static shape given in Eq. (20).

The summation is over the 168 array elements. Since all the elements are identical, all the $Q_{hole} - Q$ are the same, and only the distance to the field point, R_m, changes. It should be noted that this dynamic model neglects any acoustic coupling between the elements via mutual radiation impedances or through the connected backing cavities. Computations (not shown) were done including mutual radiation impedances as described in Porter [37]. This had little impact on the computed beampattern, due to the relatively low impedance of the air. Note that mutual radiation impedance would be much more important if operating in a heavy fluid such as water.

3. Fabrication

The cMUT sensor was fabricated with an electroplated nickel surface micromachining process. The process started with a 550 μm thick soda lime glass wafer as shown in Fig. 4 panel 1. To clean the wafer, a Piranha clean was conducted for 5 min. 75 nm/225 nm thick Cr/Au interconnects (a bottom electrode and

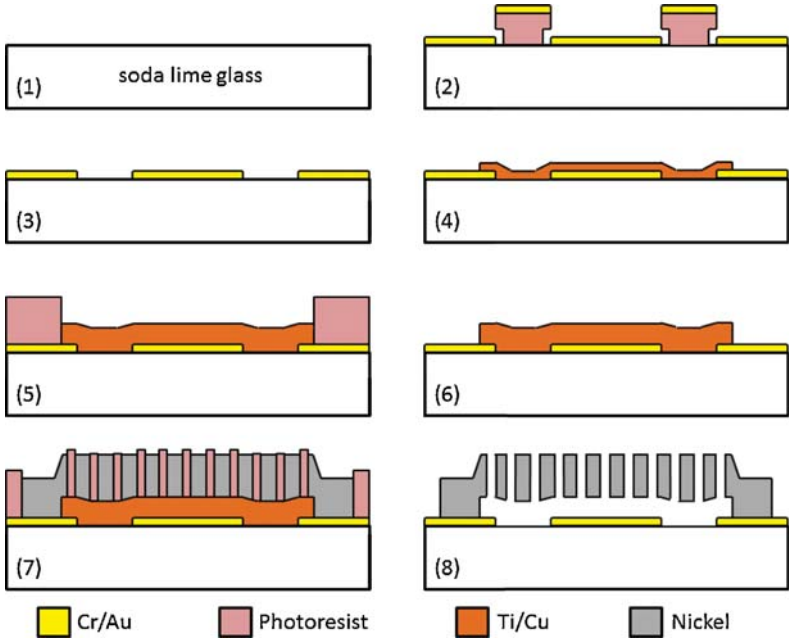

Fig. 4. Fabrication process using nickel and copper electroplating.

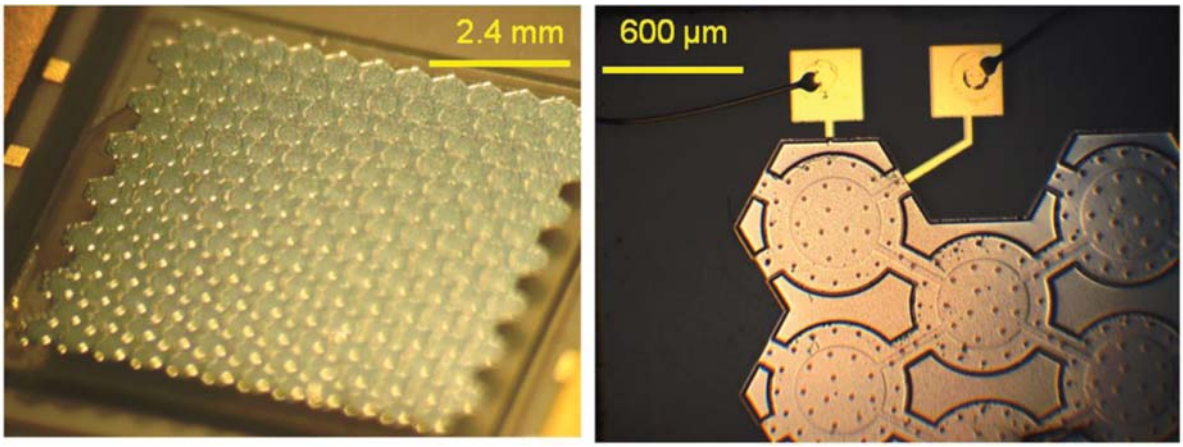

Fig. 5. Photograph of the entire nickel cMUT array after packaging (left) and a corner of the array at higher magnification (right).

bonding pads) were deposited with sputtering and patterned by liftoff using liftoff resist (LOR) as shown in Fig. 4 panels 2 and 3. Subsequently, a thin seed layer of Ti/Cu (30 nm/300 nm) was deposited in preparation for copper plating and patterned by liftoff using LOR as shown in panel 4. 8 μm thick AZ 9245 photoresist was then spun on as a mask for the plated Cu sacrificial layer, seen in panel 5. Before copper plating, the copper oxide was removed by a short dip in the Cu plating solution with no current applied. As shown in panel 6, a 5 μm sacrificial layer of copper was then electroplated to cover the entire substrate except anchor regions and contact pads in a commercial copper plating solution [Technic, Inc., Cranston, RI]. The plating solution was 5–10% copper sulfate, 15–20% sulfuric acid, with chloride ions and brightener additives. Plating was conducted at room temperature, a bath pH of 0.5, and a plating current density of approximately 5 mA/cm^2. The plating rate was 150 nm/min. After copper plating, the sacrificial layer was complete.

An AZ 9260 photoresist mold was then deposited and photopatterned. This photoresist mold defines the structural layer including the holes, as shown in panel 7. The 9 μm thick structural layer was electroplated at 50 °C in a commercial nickel sulfamate plating solution [Technic Inc., Cranston, RI], consisting of 20–35% nickel sulfamate, 0.5–1.5% nickel bromide, and 1–3% boric acid, with a pH of 4.0. The plating rate was approximately 100 nm/min and the resulting surface roughness R_a was approximately 30–40 nm. To minimize the surface roughness of the plated structure in both plating procedures, a small plating current (≈5 mA/cm^2) was used, as well as agitation and filtration of the plating solution. After nickel plating, a protective photoresist layer was spun on for dicing the wafer. Finally, the resist was stripped and the sacrificial layer was etched away in a mixture of 1 part Acetic Acid to 1 part 30% Hydrogen Peroxide to 18 parts DI water for 24 h, producing the structure seen in panel 8. The chip was then rinsed in water, isopropanol, and methanol, and finally allowed to air dry in a dry box at low relative humidity.

The chip was packaged into a 16 pin DIP package using epoxy and ball bonded with 25 μm diameter gold wire. Fig. 5 shows photographs of the finished device. Tables 1 and 2 give the target geometric and the material properties of the sensor structure. There is some deviation from the target structural layer thickness in the fabricated devices. For the transmit (TX) chip and receive (RX) chips, the measured thickness of the structural nickel was 9.5 μm ± 0.5 μm and 8.5 μm ± 0.5 μm respectively. For both chips, the thickness of the air gap was within 0.5 μm of the target thickness of 5.0 μm.

4. Electronics

The nickel-on-glass chip has a high predicted snapdown voltage of 360 V. The high snapdown voltage of the nickel-on-glass chip is due to the thick structure and the air gap. The high snapdown device can sustain a high input voltage swing on the transmitter, and a high DC bias voltage on the receiver to increase output and sensitivity if desired.

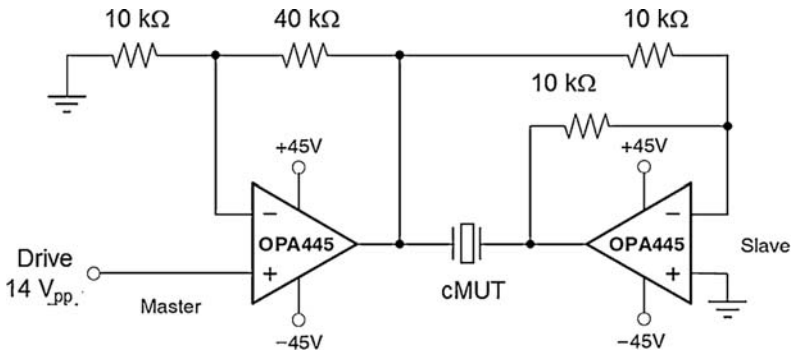

Fig. 6. Transmit bridge amplifier circuit with the cMUT chip.

Modified from [20].

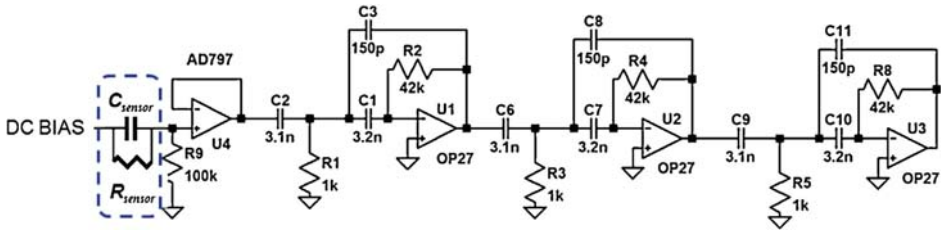

Fig. 7. Receive electronics.

In order to produce a higher voltage swing for the input, a bridge amplifier stage was used for the transmitter. A high voltage operational amplifier (OPA 445 high voltage FET-Input operational amplifier [Texas Instrument, Dallas, TX]) was used to increase the voltage swing across the cMUT to as much as 180 $V_{peak\text{-}to\text{-}peak}$ while operating from ±45 V supplies. In operation, 140 $V_{peak\text{-}to\text{-}peak}$ was used at 180 kHz due to slew rate limitations on the amplifiers. Fig. 6 shows the circuit. The drive is configured as a bridge amplifier, allowing voltage swings twice as large as the power supply range through a differential drive scheme.

The receive electronics, shown in Fig. 7, consist of a DC bias source, a voltage preamplifier, and subsequent gain stages. The DC bias of 10 V was provided using the ADR01 voltage reference IC [Analog Devices, Wilmington, MA]. In receive mode, the element acts as a current source through electrostatic coupling. With the DC bias held fixed across the element, the oscillatory current delivered to the electrical side by a single element is

$$I = \frac{\int_0^{a_2} \Psi(r) r dr}{\int_0^{a_1} \Psi(r) r dr} \frac{\varepsilon_0 V_{dc}}{g_0^2} Q \tag{27}$$

The voltage preamplifier integrates this current using the self-capacitance of the MEMS device, C_{sensor}, of 65 pF. The preamplifier is realized using the AD797 low noise operational amplifier [Analog Devices, Wilmington, MA]. A 100 kΩ DC stabilizing resistor, R_9, is included between the voltage amplifier input and ground, resulting in a high pass filter with a cutoff frequency of 25 kHz. Following the preamplifier, the signal is passed into a series of three operational amplifier based circuits, each configured with a bandwidth of 2–800 kHz and 26 dB of voltage gain. Within the passband of the system, between 25 kHz and 800 kHz, the voltage output at the end of the chain is simply

$$V_{out} = \frac{GN_2}{C_{sensor} j\omega} I \tag{28}$$

where $G = 8000$ is the voltage gain of the amplifier chain, $N_2 = 168$ is the number of cMUTs in the array, $C_{sensor} = 65$ pF is the capacitance of the chip, and I is the current delivered by an individual element, taken from Eq. (27).

Fig. 8 shows the physically realized receive electronics. The board consists of a ZIF socket for holding the packaged cMUT chip, the circuit above, and power and signal connectors. The electronics are enclosed by a grounded metal box for protection from electromagnetic interference (EMI). An optional 90 V DC bias source is also included, although due to thermal problems the higher DC bias was not used.

Using the model with the best fit structural impedance values of Table 3, and the electronics as described here, the transmitted pressure and receive sensitivity for these two chips can be computed. The results are shown in Fig. 9. The on-axis sound pressure level at 1 m from the transmit array is 69 dB SPL, when driving with 140 V_{pp} at 180 kHz (14 V_{pp} at the input to the bridge amplifier).

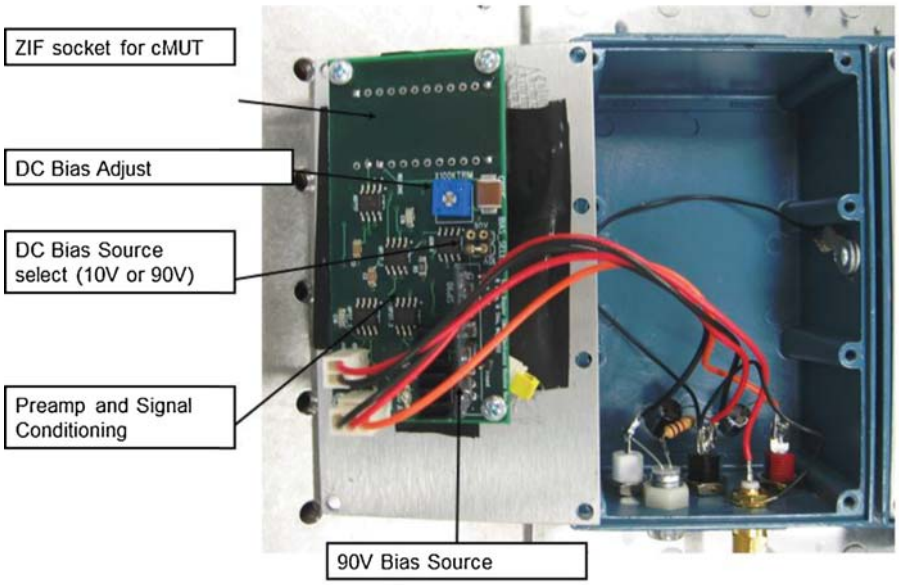

Fig. 8. Physical realization of the receive electronics.

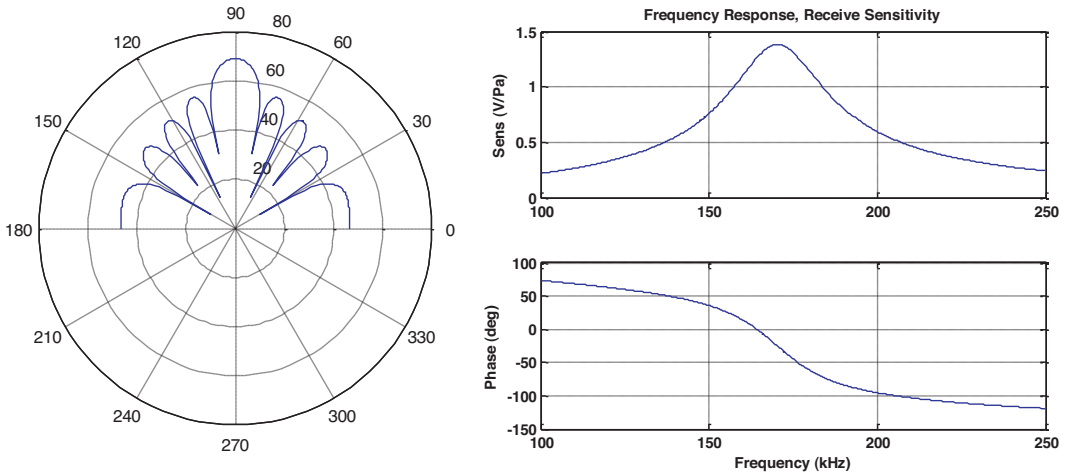

(a) (b)

Fig. 9. Predicted array performance using the best fit structural impedance from Table 3. (a) Predicted farfield transmit beampattern at 180 kHz for the transmit array at a distance 1 m from the center of the array. Results are for 140 V_{pp} drive, and are presented in dB SPL (dB re 20 μPa_{rms}). (b) Predicted receive array sensitivity. Results are reported at the end of the amplifier chain (output of U3 in Fig. 7) with 10 V_{dc} bias and for a normally incident plane wave.

This requires ±35 V supplies for the bridge amplifier circuit. Note that 180 kHz is not exactly matched to the transmit array peak, so higher outputs could be generated if driving exactly at the chip peak frequency. The predicted −3 dB beamwidth for this calculation is 11.4° (5.7° on either side of center). The peak sensitivity for the receive array for a normally incident plane wave with a 10 V_{dc} bias applied is 1.38 V/Pa at 170 kHz. The predicted receive array response at 180 kHz is 1.14 V/Pa.

5. Experimental results

The driven frequency responses of all 168 elements in the transmit and receive arrays were measured using LDV, producing frequency response plots similar to that seen in Fig. 3. For the receiver chip, the average value of the resonant frequency of 168 elements is 158.56 kHz and the standard deviation is 4.96 kHz, with 166/168 yield. For the transmitter chip, the average value of the resonant frequency of 168 elements is 188.40 kHz and the standard deviation is 10.06 kHz with 163/168 element yield. For highest performance, element yield should be high, and the resonant frequencies should all be well matched. As shown experimentally, the achieved yield and matching is sufficient for long-range operation. However, improving yield and tightening tolerances on the resonant frequency would result in improved performance.

A free field measurement was conducted using the pair of cMUT chips. The transmitter produced a continuous wave acoustic signal at 180 kHz. The receive array was 10 cm away and always oriented directly toward the transmit array. The transmit array was rotated in place using a micrometer rotation stage. The RMS receive response at the drive frequency was recorded at each angle. Fig. 10 shows a comparison between the measured and modeled beampattern for the pair. The agreement is very good, showing a −3 dB half beamwidth of approximately 6° as predicted by the model. The first sidelobes are down approximately −15 dB as expected.

In operation, there is the need for electromagnetic interference (EMI) protection to prevent RF communication between the transmit and receive electronics. In order to accomplish this, the cMUT array chips and electronics are mounted in grounded metal boxes with shielded signal lines, as shown in Fig. 11.

To investigate the achievable range of the system, range testing was conducted using continuous wave acoustics at 180 kHz, as shown in Fig. 12. The drive signal was 14 V_{pp} to the bridge amplifier at 90 kHz, resulting in acoustics at 180 kHz due to the square law electrostatics. The DC bias on the receiver side was 10 V. The nickel-on-glass chip has their angle fixed during range testing. Three reflector materials were used: plywood, aluminum, and acrylic. The reflector was oriented orthogonal to the transmit/receive main axis.

Experimental results show a maximum range of 1.5 m as shown Fig. 13. Received signal power decreases with distance according to the expected law including geometric spreading and acoustic absorption [32],

$$EL = SL_{50\ \mathrm{cm}} - (7\ \ \mathrm{dB/m})(2D - 50\ \ \mathrm{cm}) - 6\ \ \mathrm{dB}\ \ \log_2(D/50\ \ \mathrm{cm}) \quad (29)$$

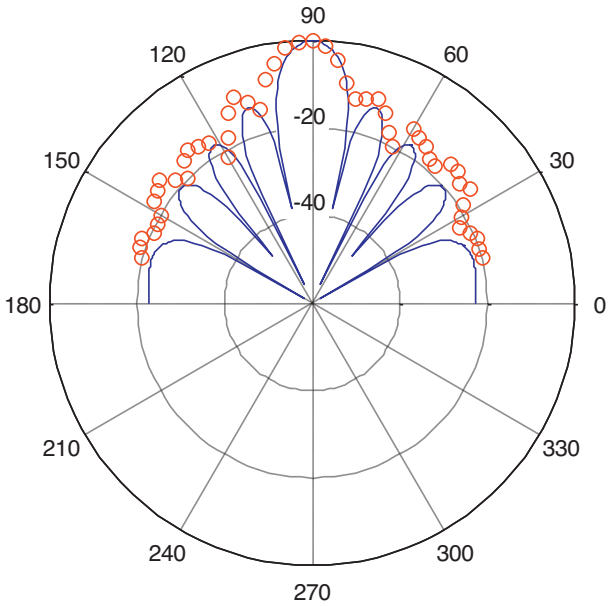

Fig. 10. Comparison between the modeled (solid line) and measured (open circles) beampattern for the transmit/receive array in a free field test. Normalized to maximum pressure (0 dB at peak).

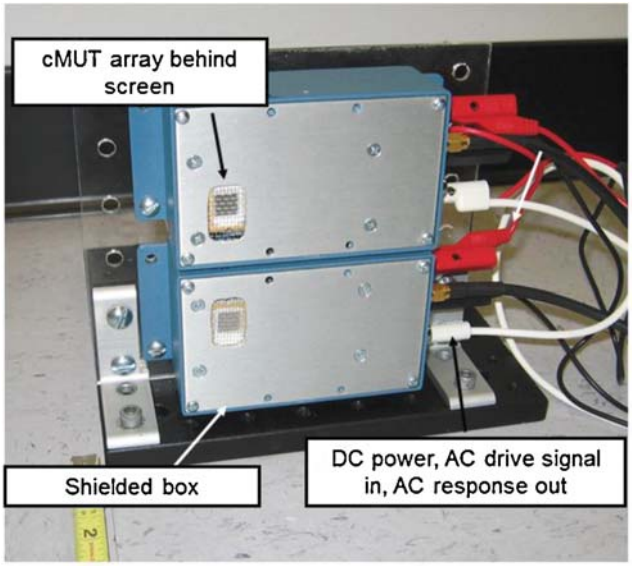

Fig. 11. Photograph of the transmit/receive system including shielding boxes.

where EL is the received echo level in dB, $SL_{50\,cm}$ is the source level at 50 cm, taken from the measured data. *7* dB/m is the single direction acoustic absorption in air at 180 kHz, and *6* dB is the geometric spreading per doubling of distance between the source and reflector. Note that this is *6* dB rather than *3* dB since there is a two directional travel. *D* is the distance between the source/receiver and the reflector.

With $D \geq 1.5$ m, the signal decreases below the background reverberation level ($-67\,dB\,V_{rms}$). Each material has the similar range results. The noisefloor in the diagram is the electronic noisefloor. Noise level is always dependent on sampling. In this experiment, the sampling frequency was $F_s = 1$ MHz and the number of samples was 2^{20}, resulting in a total data acquisition time of 1.0 s per point.

Finally, a computer controlled velocity sled was used to demonstrate measurable Doppler shifts, as shown in Fig. 14. Control of the sled velocity was accomplished using a DC motor and optical shaft encoder. Continuous acoustic waves were again generated by a stationary transmit array at 180 kHz, reflected off of the moving aluminum plate at various velocities, and received by the stationary receive array. The distance to the reflector varies during the test. At its closest approach the reflector is 3 cm from the sensors. At its most distant, the reflector is 1 m away. For velocity comparison, a laser fiber optic velocimeter was used, also reflecting off of the moving plate.

The Doppler shift for a stationary transmitter/receiver and moving reflector, at speeds well below the speed of sound, is [32]

$$\Delta f = f_c \frac{2v}{c} \tag{30}$$

where $f_c = 180$ kHz is the carrier frequency, v is the velocity of the reflector relative to the transmit/receive arrays, and c is the speed of sound. A positive Doppler shift indicates motion of the reflector toward the transducers, and a negative Doppler shift indicates motion away.

Fig. 15 shows spectrograms of the received ultrasonic signal for various motions of the reflector. Data was captured at *1 MHz*, with the total number of sampling points $N = 2^{20}$, corresponding to approximately 1 s of data. The spectrogram uses a 2^{14} point Hamming window with 50% overlap. This is a time window of 0.016 s, thus the minimum resolvable shift in frequency is $\Delta f = 61$ Hz which corresponds to a velocity resolution of 5.8 cm/s. The spectrograms are presented with the frequency shift noted on the left axis, and the corresponding velocity v from Eq. (30) on the right axis.

The white dashed line in each plot shows the velocity as measured by LDV. In the LDV data, there are missing points and drop outs due to poor reflection at some times. The Doppler measurement of velocity from the cMUT does not exhibit this problem. The velocity profile measured by the cMUT Doppler matches the LDV data very well. The velocity command sent to the motor controller is noted in each panel of the figure, although it is clear from both the cMUT and LDV data that there is considerable true variation of the plate velocity around the setpoint, including vibrations of the plate.

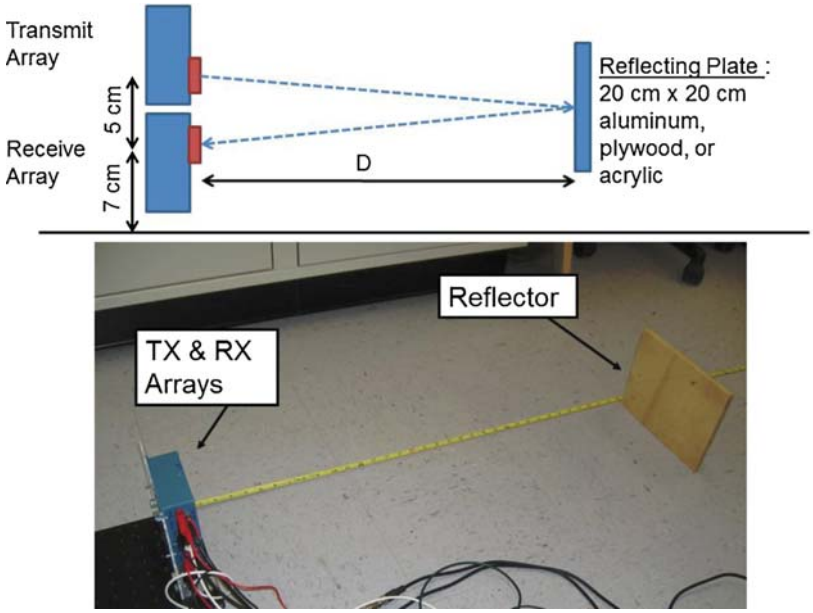

Fig. 12. Diagram and photograph of the range measurement test set up.

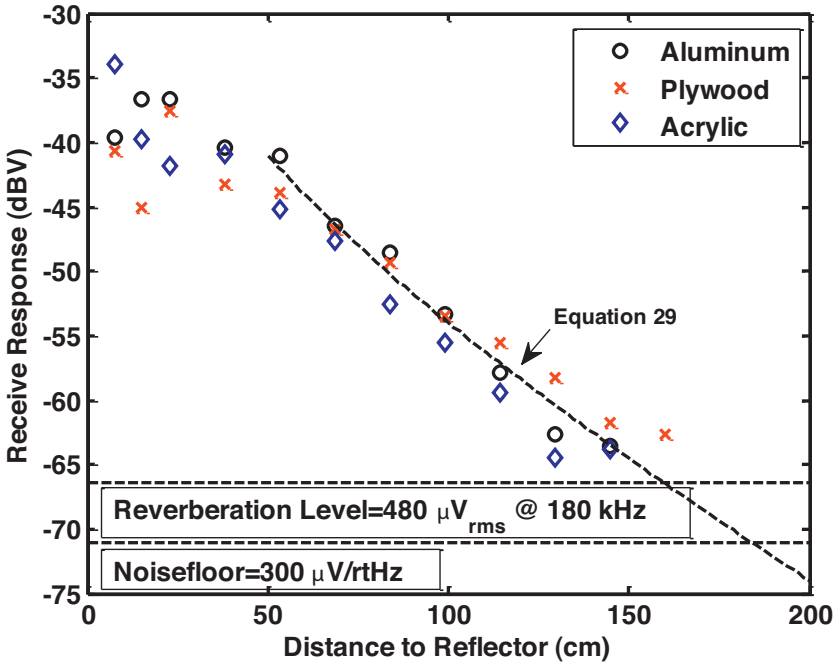

Fig. 13. Range test result using cMUT array with three reflection materials such as aluminum, plywood, and acrylic.

Fig. 15(a) shows a rapid motion of the plate toward the arrays. Considerable vibration and velocity variation of the plate are observed. These are real motions of the plate and are accurately captured by both the ultrasonic and LDV systems. An excellent match is obtained between the two measurement methods. It is clear from the figure also that the received response becomes louder as the reflector approaches, as expected. Fig. 15(b) shows a case of the reflector moving toward the sensor at a low speed. In this panel, the resolution of velocity due to the finite time window is evident. When using a 16 ms time window, as was done here, the frequency resolution in the FFT is equivalent to a 5.8 cm/s velocity resolution. Fig. 15(c) shows a case of the reflector moving away from the sensor at an intermediate speed. In the spectrogram, there are 'ghost' bands at harmonics of the shifted frequency. These were most noticeable in data where the reflector was moving away from the arrays. This phenomenon is likely caused by multiple reflections between the transmit/receive arrays and the reflector. Fig. 15(d) is an example of an intermediate speed movement toward the sensors with many similarities to panel (a).

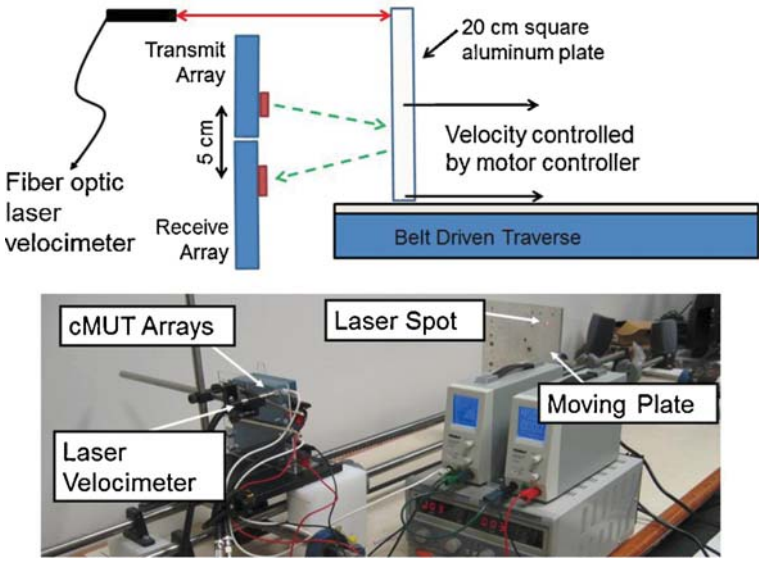

Fig. 14. Diagram and photograph of the test set up used for measuring Doppler velocity response of the system.

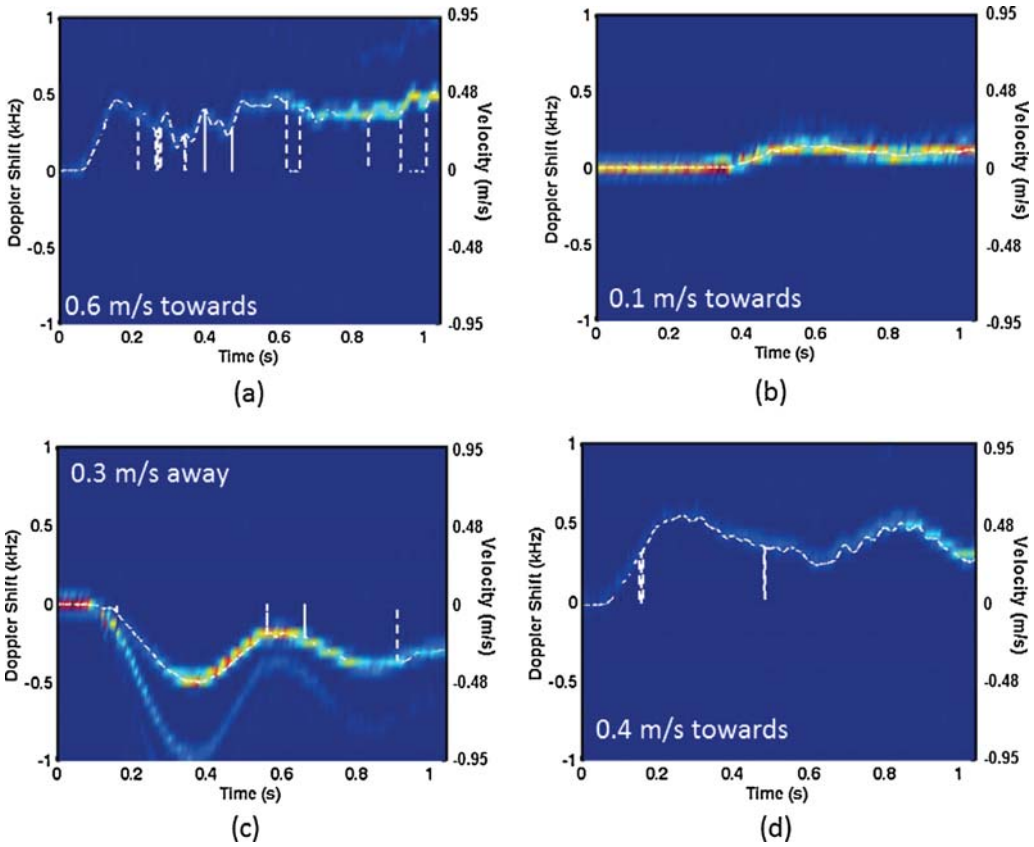

Fig. 15. Spectrograms of the received ultrasound signal presented as a Doppler shift away from the carrier frequency of 180 kHz. The corresponding velocity computed from Eq. (30) is given on the right axis. The dashed white line shows the velocity measured by the laser velocimeter.

6. Conclusion

An ultrasonic velocity sensor using MEMS technology is explored as a navigational sensor. The system works off of a different sensing modality than other rangefinding sensors such as laser, RF RADAR, or infrared rangefinders. The nickel-on-glass chip was fabricated with a low cost 3 layer nickel-on-glass surface micromachining process. The process is simple to apply with no high performance material layers that must be carefully tuned. A computational model has been developed that predicts many of the features of the system response, including excellent models of absolute system output, damping, bandwidth, and array beampattern.

The system operates at 180 kHz in a continuous wave modality. Beampattern measurements show a 12° −3 dB beamwidth (6° either side of center). The sidelobes are 15 dB below the main lobe. These results agree with theoretical models. The beamwidth of the system is considerably narrower than most other ultrasonic rangefinders on the market, which may reduce problems with multipath reflections. This claim needs further verification.

A velocity sled was constructed and used to demonstrate measurable Doppler shifts at varying velocities. The Doppler shifts match very well with laser velocimetry measurements of a moving aluminum plate at velocities up to 0.5 m/s. The velocity resolution is approximately 6 cm/s in a 60 Hz band (60 velocity updates per second). Velocity resolution and time resolution can be traded off dynamically. By using a longer time window and thereby reducing temporal resolution, velocity resolution can be increased. This tradeoff can be managed flexibly during signal processing.

Future work on this system will consider frequency modulated operation for distance measurement, and characterization with acoustic reflectors that may be relevant for navigation problems. The system will be further miniaturized and integrated with a robotic platform for demonstration as an alternative navigational sensor.

Acknowledgement

This work was funded by the Draper Labs University Research and Development Program.

References

[1] Y. Ando, S. Yuta, Following a wall by an autonomous mobile robot with a sonar-ring, Proceedings of 1995 IEEE International Conference on Robotics and Automation 1–3 (1995) 2599–2606.
[2] J.A. Castellanos, J.M. Martinez, J. Neira, J.D. Tardos, Simultaneous map building and localization for mobile robots: a multisensor fusion approach, 1998 IEEE International Conference on Robotics and Automation 1–4 (1998) 1244–1249.
[3] G. Hueber, T. Ostermann, T. Bauernfeind, R. Raschhofer, R. Hagelauer, New approach of ultrasonic distance measurement technique in robot applications, in: 2000 5th International Conference on Signal Processing Proceedings, vols. I–III, 2000, pp. 2066–2069.
[4] C.Y. Lee, H.G. Choi, J.S. Park, K.Y. Park, S.R. Lee, Collision avoidance by the fusion of different beam-width ultrasonic sensors, in: 2007 IEEE Sensors, vols. 1–3, 2007, pp. 985–988.
[5] O. Manolov, S. Noikov, P. Bison, G. Trainito, Indoor mobile robot control for environment information gleaning, in: Proceedings of the IEEE Intelligent Vehicles Symposium, 2000, pp. 602–607.
[6] G.C. Anousaki, K.J. Kyriakopoulos, Simultaneous localization and map building for mobile robot navigation, IEEE Robotics & Automation Magazine 6 (1999) 42–53.

[7] J.A. Jimenez, J. Urena, M. Mazo, A. Hernandez, E. Santiso, Three-dimensional discrimination between planes, corners and edges using ultrasonic sensors, in: Proceedings of the IEEE Conference on Emerging Technologies and Factory Automation, 2003, vol. 2, ETFA'03, 2003, pp. 692–699.
[8] M. Alwan, M.B. Wagner, G. Wasson, P. Sheth, Characterization of infrared range-finder PBS-03JN for 2-D mapping, in: Proceedings of the 2005 IEEE International Conference on Robotics and Automation, ICRA, 2005, pp. 3936–3941.
[9] K. Heon-Hui, H. Yun-Su, J. Gang-Gyoo, A study on the environmental map building for a mobile robot using infrared range-finder sensors, in: Proceedings of IEEE/RSJ International Conference on Intelligent Robots and Systems, 2003, vol. 1, IROS, 2003, pp. 711–716.
[10] R. Przybyla, S. Shelton, A. Guedes, R. Krigel, D. Horsley, B. Boser, In-air ultrasonic rangefinding and angle estimation using an array of AlN micromachined transducers, in: Proc. Hilton Head Solid-State Sensors, Actuators and Microsystems Workshop, 3–7 June, 2012, pp. 50–53.
[11] C. Kuratli, H. Qiuting, A CMOS ultrasound range finder microsystem, in: IEEE International Solid-State Circuits Conference 2000. Digest of Technical Papers, vol. 455, ISSCC, 2000, pp. 180–181.
[12] K.Y. Lee, N. LaBianca, S.A. Rishton, S. Zolgharnain, J.D. Gelorme, J. Shaw, T.H.-P. Chang, Micromachining applications of a high resolution ultrathick photoresist, Journal of Vacuum Science & Technology B: Microelectronics and Nanometer Structures 13 (1995) 3012–3016.
[13] C.-H. Ho, K.-P. Chin, C.-R. Yang, H.-M. Wu, S.-L. Chen, Ultrathick SU-8 mold formation and removal, and its application to the fabrication of LIGA-like micromotors with embedded roots, Sensors and Actuators A: Physical 102 (2002) 130–138.
[14] V.D. Samper, A.J. Sangster, R.L. Reuben, U. Wallrabe, Multistator LIGA-fabricated electrostatic wobble motors with integrated synchronous control, Journal of Microelectromechanical Systems 7 (1998) 214–223.
[15] M. Despont, H. Lorenz, N. Fahrni, J. Brugger, P. Renaud, P. Vettiger, High-aspect-ratio, ultrathick, negative-tone near-UV photoresist for MEMS applications, in: Proceedings of IEEE Micro Electro Mechanical Systems, MEMS, 1997, pp. 518–522.
[16] C.B. Doody, C. Xiaoyang, C.A. Rich, D.F. Lemmerhirt, R.D. White, Modeling and characterization of CMOS-fabricated capacitive micromachined ultrasound transducers, Journal of Microelectromechanical Systems 20 (2011) 104–118.
[17] M. Bauccio, American Society for Metals, ASM Metals Reference Book, 3rd ed., ASM International, Materials Park, OH, 1993.
[18] J.K. Luo, S.M. Spearing, N.A. Fleck, W.I. Milne, Young's modulus of electroplated Ni thin film for MEMS applications, Materials Letters 58 (2004).
[19] M.J. Madou, Fundamentals of Microfabrication: The Science of Miniaturization, CRC Press, Boca Raton, FL, 2002.
[20] Texas Instrument, High Voltage FET-Input Operational Amplifier OPA445 Manual.
[21] Z. Zhao, J. Gallman, R.D. White, A MEMS floating element with bump shear stress sensor array on a chip, in: Proceedings of the 51st AIAA Aerospace Sciences Meeting, January 7–10, Grapevine, TX, 2013.
[22] O. Ahrens, A. Buhrdorf, D. Hohlfeld, L. Tebje, J. Binder, Fabrication of gap-optimized CMUT, IEEE Transactions on Ultrasonics, Ferroelectrics and Frequency Control 49 (2002) 1321–1329.
[23] L.L. Beranek, Acoustics, American Institute of Physics for the Acoustical Society of America, New York, NY, 1986.
[24] C. Biber, S. Ellin, E. Shenk, J. Stempeck, The polaroid ultrasonic ranging system, in: Audio Engineering Society Convention, 1980.
[25] G. Caliano, R. Carotenuto, A. Caronti, M. Pappalardo, cMUT echographic probes: design and fabrication process, IEEE Ultrasonics Symposium 2 (2002) 1067–1070.
[26] P.C. Eccardt, K. Niederer, T. Scheiter, C. Hierold, Surface micromachined ultrasound transducers in CMOS technology, IEEE Ultrasonics Symposium 2 (1996) 959–962.
[27] W.J. Fleming, New automotive sensors—a review, IEEE Sensors Journal 8 (2008) 1900–1921.
[28] M. Greenspan, Piston radiator: some extensions of the theory, Journal of the Acoustical Society of America 65 (1979) 608.
[29] M.I. Haller, B.T. Khuri-Yakub, A surface micromachined electrostatic ultrasonic air transducer, IEEE Transactions on Ultrasonics, Ferroelectrics and Frequency Control 43 (1996) 1–6.
[30] D. Homentcovschi, R.N. Miles, Viscous damping of perforated planar micromechanical structures, Sensors and Actuators A: Physical 119 (2005) 544–552.
[31] X. Jin, I. Ladabaum, B.T. Khuri-Yakub, The microfabrication of capacitive ultrasonic transducers, Journal of Microelectromechanical Systems 7 (1998) 295–302.
[32] L.E. Kinsler, A.R. Frey, A.B. Coppens, J.V. Sanders, Fundamentals of Acoustics, 4th ed., John Wiley and Sons, New York, NY, 2000.
[33] I. Ladabaum, X. Jin, H.T. Soh, A. Atalar, B.T. Khuri-Yakub, Surface micromachined capacitive ultrasonic transducers, IEEE Transactions on Ultrasonics, Ferroelectrics and Frequency Control 45 (1998) 678–690.
[34] M. Lax, The effect of radiation on the vibrations of a circular diaphragm, Journal of the Acoustical Society of America 16 (1944) 5–13.
[35] D.F. Lemmerhirt, X. Cheng, R.D. White, C.A. Rich, M. Zhang, J. Fowlkes, O.D. Kripfgans, A 32×32 capacitive micromachined ultrasonic transducer array manufactured in standard CMOS, IEEE Transactions on Ultrasonics, Ferroelectrics and Frequency Control 59 (2012) 1521–1536.
[36] N.V. Myung, D. Park, B. Yoo, P.T. Sumodjo, Development of electroplated magnetic materials for MEMS, Journal of Magnetics and Magnetic Materials 265 (2003) 189–198.
[37] D.T. Porter, Self- and mutual-radiation impedance and beam patterns for flexural disks in a rigid plane, Journal of the Acoustical Society of America 36 (1964) 1154–1161.
[38] M. Shin, J.S. Krause, P. DeBitetto, R.D. White, Acoustic Doppler velocity measurement system using capacitive micromachined ultrasound transducer array technology, Journal of the Acoustical Society of America 134 (2) (2013) 1011–1020.
[39] Z. Skvor, On acoustical resistance due to viscous losses in the air gap of electrostatic transducers, Acustica 19 (1967) 295–297.
[40] K. Yamashita, K. Iwahashi, Y. Ohmura, M. Okuyama, Ultrasonic position measurement using phased array microsensors with resonant frequency variation, IEEE Solid-State Sensors, Actuators and Microsystems Conference, Transducers'07 (2007) 1271–1274.
[41] J.N. Reddy, Theory and Analysis of Elastic Plates and Shells, CRC Press, Boca Raton, FL, 2007.
[42] T.J.R. Hughes, The Finite Element Method, Dover Publications, New York, 2000.
[43] B.A. Finlayson, L.E. Scriven, The method of weighted residuals—a review, Applied Mechanics Reviews 19 (1966) 735–738.
[44] B.A. Finlayson, The Method of Weighted Residuals and Variational Principles, Academic Press, New York, 1972.